JVST A
Journal of Vacuum Science & Technology A
ARTICLE
pubs.aip.org/avs/jva

Effects of the focus ring on the ion kinetics at the wafer edge in capacitively coupled plasma reactors

Cite as: J. Vac. Sci. Technol. A **41**, 053002 (2023); doi: 10.1116/6.0002585
Submitted: 13 February 2023 · Accepted: 30 June 2023 ·
Published Online: 27 July 2023

View Online

Export Citation

CrossMark

Fang-Fang Ma,[1] Quan-Zhi Zhang,[1,a)] Dao-Man Han,[2] Zi-Lan Xiong,[3] Ming Gao,[4] and You-Nian Wang[1]

AFFILIATIONS

[1]School of Physics, Dalian University of Technology, Dalian 116024, People's Republic of China
[2]Lab of Advanced Space Propulsion and Beijing Engineering Research Center of Efficient and Green Aerospace Propulsion Technology, Beijing Institute of Control Engineering, Beijing 100190, People's Republic of China
[3]State Key Laboratory of Advanced Electromagnetic Engineering and Technology, Huazhong University of Science and Technology, Wuhan 430000, People's Republic of China
[4]Shenzhen Institute of Advanced Technology, Chinese Academy of Sciences, Shenzhen 518055, People's Republic of China

[a)]**Author to whom correspondence should be addressed:** qzzhang@dlut.edu.cn

28 July 2023 00:26:18

ABSTRACT

The fabrication process of modern microelectronic devices faces a significant challenge regarding the uniformity of wafer processing during plasma etching. Particularly, nonuniformity is prominent at the wafer edge due to varying electrical properties, leading to sheath bending and distorted ion trajectories. To address this issue, a wafer terminating structure known as a focus ring is employed to modify the sheath structure near the edge of the wafer and ensure uniform ion fluxes. However, the focus ring is subject to erosion caused by the plasma, making it crucial to minimize the ion energy bombarding the focus ring. In light of this, this paper investigates the impact of parameters such as the wafer-focus ring gap, focus ring height, and dielectric constant of the focus ring on the ion angle onto the wafer and the ion energy onto the focus ring. To conduct the analysis, a 2D3V particle-in-cell/Monte Carlo collision model is utilized. The study reveals the existence of horizontal electric fields with opposite directions at the wafer edge and the inner edge of the focus ring. Optimizing the ion angle onto the wafer edge can be achieved by adjusting the material and geometry of the focus ring. Furthermore, reducing the ion energy at the focus ring can be accomplished by increasing the height or decreasing the dielectric constant of the focus ring.

Published under an exclusive license by the AVS. https://doi.org/10.1116/6.0002585

I. INTRODUCTION

Radio frequency (RF) capacitively coupled plasma (CCP) technology has been widely applied in the semiconductor manufacturing industry. In order to reduce the manufacturing costs of semiconductor devices, wafers with ever-larger diameters have been utilized.[1–3] However, the biggest challenge for large wafers is delivering a highly uniform etch to make trillions of identical chip cells.[3,4]

Generally, the surface of materials exposed to plasma may consist of various conductors and dielectrics.[5] The different materials lead to variations in plasma density and sheath potential due to each insulating nature.[5–7] In particular, the distortion of the sheath potential in a small region near the material interface results in a skewed ion impact angle on the surface.[8,9] Besides, the height of the materials may also be different, which adjusts the impedance of the insulator, affecting the degree of distortion of the sheath.[10–12] In particular, the changes in electrical properties caused by sharp edges and material transitions of the substrate often make the outer portion of the wafer unusable for producing devices due to sheath bending and nonuniform ions angular distribution function (IADF) and ions energy distribution function (IEDF).[3,5,13,14]

To alleviate the distortion of the sheath near the wafer edge and improve the uniformity of IEDF and IADF,[15–17] a focus ring is usually connected to the edge of the substrate structure to provide

Published under an exclusive license by the AVS

smooth transitions. A small gap (about hundreds of micrometers to a few mm) between the wafer and the focus ring is often set to facilitate placement and removal of the wafer.[18] The modulation of wafer-focus ring gap, dielectric constant, and height of the focus ring, is, therefore, expected to affect the sheath shape and plasma properties around the edge of the wafer.

Kim *et al.*[19] studied the ion fluxes over the wafer edge and the focus ring, with the variations of the material and geometry of the focus ring at the pressure of a few Torr. They proposed that more uniform deposition film at the wafer edge can be achieved by using a small wafer-focus ring gap and a high focus ring. Babaeva and Kushner[18] further found the penetration of plasma into the wafer-focus ring gap increases as the gap size approaches and exceeds the Debye length. They also depicted that the dielectric constant and the height of the focus ring significantly influence the ion energy and angular distributions incident into the wafer-focus ring gap.[20]

Furthermore, Wang *et al.*[15] found that as the dielectric constant decreases, both the focus ring capacitance and the voltage across the sheath reduce, producing lower-energy ions bombarding the focus ring. This can avoid the erosion of the focus ring and prolong the life cycle of the focus ring.

The study of plasma discharges at low pressures is necessary to obtain vertically anisotropic etching profiles. Besides, nearly collisionless ions in the sheath are extremely sensitive to local electric field variations, which are strongly related to the structure of the focus ring. In many previous simulation studies, the effects of the focus ring on IEDF and IADF at low pressure were mainly examined by using the hybrid plasma equipment model,[18–20] where the sheath is calculated by the fluid model and the IEDF/IADF is consequently simulated by the Monte Carlo method using sampling statistical theory. However, the particle-in-cell/Monte Carlo collision (PIC/MCC) model, which calculates sheath potential, particle energy, and angle distributions self-consistently, is attractive for capturing the interactions between plasma and focus ring structure. Therefore, the systematical study of ion kinetics is highly anticipated at low pressure, based on the PIC/MCC model.

In this work, we study the effects of the focus ring height, the dielectric constant of the focus ring, and the wafer-focus ring gap on the IADF on the wafer and IEDF onto the wafer edge and focus ring in low-pressure CCP, based on the 2D3V (i.e., two-dimensional in space and three-dimensional in velocity space) electrostatic PIC/MCC model. It was found that the sheath is distorted near the wafer-focus ring gap, resulting in two separate electric fields at the wafer edge and the inner edge of the focus ring. The IADF and IEDF near the wafer-focus ring gap can be, thus, modulated to a large extent by adjusting the material and geometry of the focus ring.

Section II mainly introduces the model details. The simulation results and discussions are presented in Sec. III. Finally, the conclusions are given in Sec. IV.

II. IMPLEMENTATION OF THE SIMULATION

A cylindrical coordinate 2D3V implicit electrostatic PIC/MCC code is used to perform the study of this work, which has been described in detail by Wang *et al.*[21] The reactor geometries are shown in Fig. 1, which is $r = 12.7$ cm in radius and $z = 2.5$ cm in height. The wafer "A" (relative dielectric constant $\varepsilon_{rA} = 4$) with the

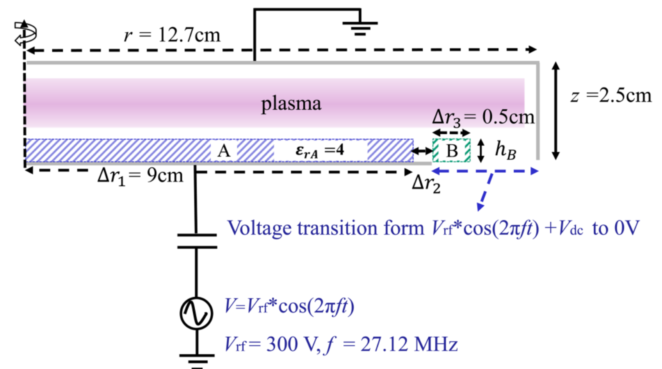

FIG. 1. Schematic of the reactor geometry.

thickness of $h_A = 0.39$ cm and the radius of $\Delta r_1 = 9$ cm is placed on the electrode. The focus ring "B" with $\Delta r_3 = 0.5$ cm is adjacent to the bottom electrode, and the gap Δr_2 between the wafer and the focus ring is adjustable. In this work, we studied the variations in the gap Δr_2 between the focus ring and the wafer (0.39, 2, 3, and 5 mm), the height of the focus ring h_B (1.95, 3.90, 5.08, and 7.80 mm), and the relative dielectric constant of the focus ring ε_{rB} (2, 6, 20, and 40). The cylindrical chamber is grounded, and an RF-power source is applied to the bottom electrode through a blocking capacitor. A DC self-bias voltage develops due to the geometrical asymmetry of the reactor, as charges will accumulate on the capacitor to ensure that the net current to the two electrodes is zero within one low-frequency RF period.[22,23] The self-bias voltage is calculated by using Vahedi's method.[24,25] Figure 2 shows the voltage waveform on the electrode and the plasma current computed by the PIC model for the cases without [Figs. 2(a) and 2(b)] and with the capacitor [Figs. 2(c) and 2(d)]. When the capacitor is omitted from the model, high-order harmonic oscillations with moderate amplitude are observed in Fig. 2(b) due to the nonlinear sheath oscillations,[26–29] whereas a DC self-bias of −160 V [obtained by averaging the voltage over one RF period in Fig. 2(c)] develops after considering the capacitor, which induces a larger sheath at the bottom electrode, resulting in an additional asymmetry and altering the overall potential distribution (Fig. 5) and density distribution (Fig. 4) in the reactor. The larger sheath promotes the nonlinear sheath oscillations at the bottom electrode, resulting in augmented harmonics in the current [Fig. 2(d)] with a larger amplitude.[27,30] Furthermore, the capacitor introduces an additional phase lag between the current and voltage, as it takes some time for the charge on the capacitor to establish a corresponding voltage, when the current flows through the capacitor, as shown in a comparison of Figs. 2(b) and 2(d).

The Neumann boundary condition is applied to the symmetric boundary at $r = 0$ (i.e.,$\nabla\varphi = 0$). Dirichlet boundary conditions are used for other boundaries: the potentials of the top electrode and chamber sidewall are fixed values of 0 V, and the bottom electrode is set to the sum of the RF and DC self-bias voltage. In the gap between the bottom electrode and the chamber sidewall, the potential is assumed to be interpolated based on a logarithm

28 July 2023 00:26:18

Published under an exclusive license by the AVS

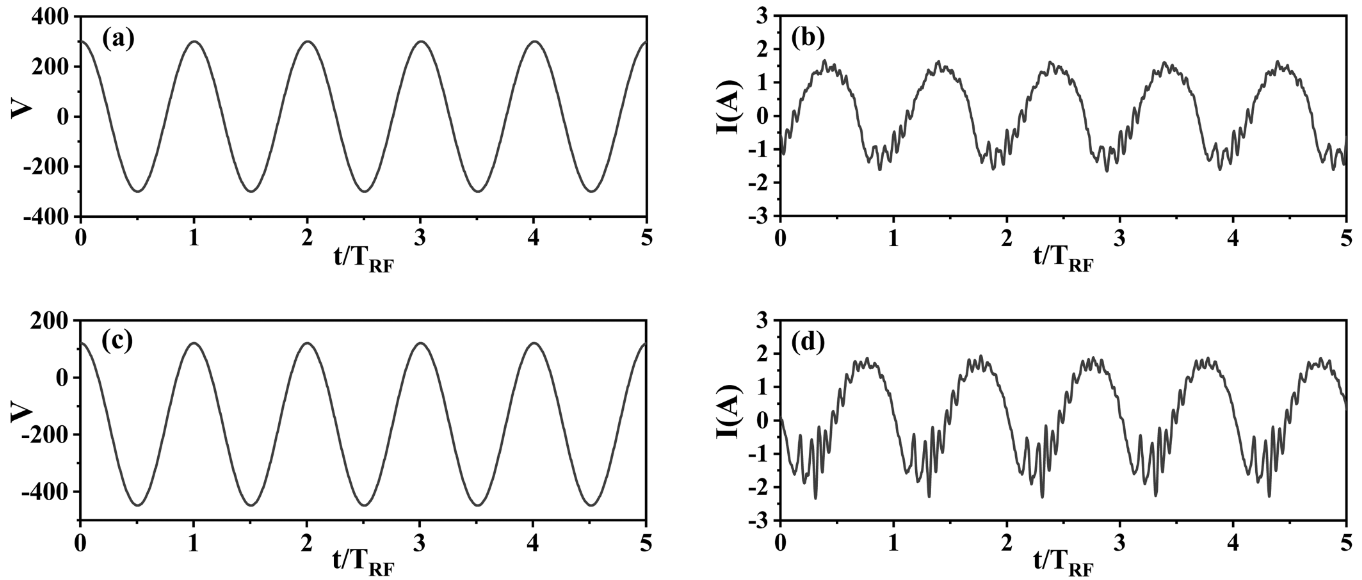

FIG. 2. (a) The voltage waveform on the electrode and (b) the plasma current without the capacitor; (c) the voltage waveform on the electrode and (d) the plasma current with the capacitor.

algorithm [i.e., the voltage transition from $V\cos(2\pi ft) + V_{DC}$ to 0].[21,31,32] To better understand the potential distribution on the bottom electrode, the time-averaged potential along the radial direction at the bottom of the chamber is shown in Fig. 3(a). The potential on the bottom electrode is −160 V at $r = 0$–9 cm (i.e., DC self-bias voltage) and gradually decays from $r = 9$ cm to $r = 12.7$ cm. Additionally, we also present the time-averaged potential distributions along the radial direction at the surface height of the focus ring for various relative dielectric constants in Fig. 3(b). It can be observed that the time-averaged potentials above the electrode mostly hover around −50 V. However, the potentials on the focus ring surface (indicated by the red dashed lines) exhibit significant variations depending on the dielectric constants. These variations are a result of changes in the impedance of the focus ring.[15] The potential difference between the wafer and the focus ring creates an additional electric field, which modulates the density, IEDF, and IADF near the edge of the electrode.

The gas is pure argon with a temperature fixed at 300 K and a pressure at 20 mTorr. The electron and ion temperatures are set as 2 and 0.026 eV, respectively, at the beginning of simulation. The contribution from excited states is negligible at lower pressures.[33,34] Electrons and Ar^+ ions are traced in the code. The reaction mechanism includes three types of e-Ar collisions: elastic ($e + Ar \rightarrow e + Ar$), excitation ($e + Ar \rightarrow e + Ar^*$), and ionization

28 July 2023 00:26:18

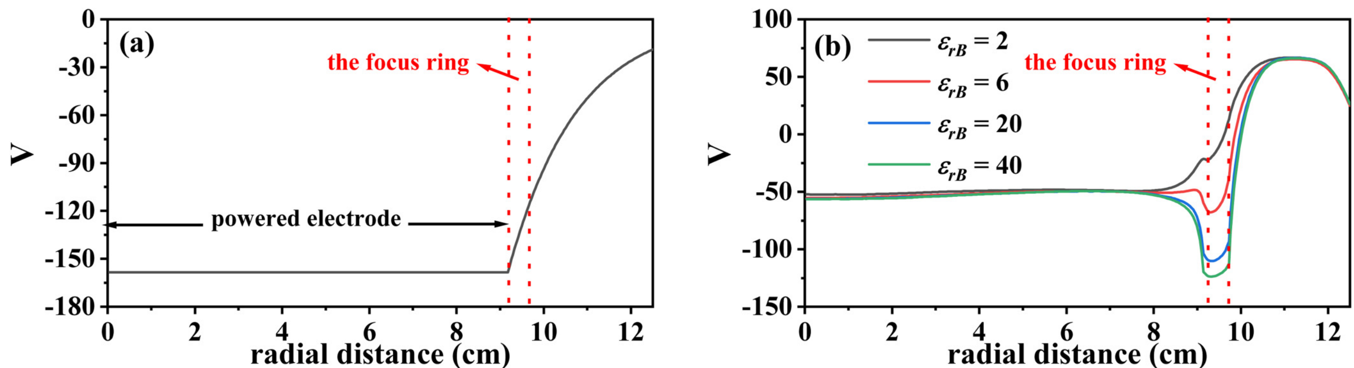

FIG. 3. Time-averaged potentials along the radial direction: (a) at the bottom of the chamber and (b) at $z = 5.85$ mm with the relative dielectric constants of $\varepsilon_{rB} = 2, 6, 20,$ and 40 for the gap $\Delta r_2 = 2$ mm and the height of the focus ring $h_B = 5.85$ mm.

Published under an exclusive license by the AVS

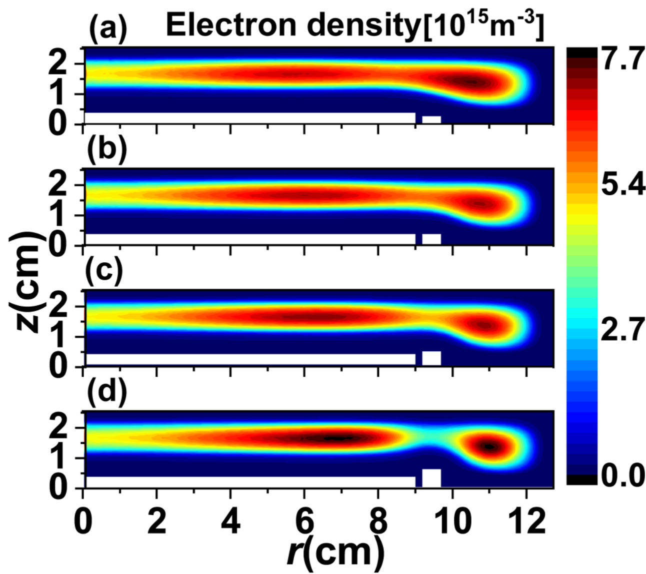

FIG. 4. Time-averaged profiles of (a)–(d) the electron density are shown with the focus ring heights of $h_B =$ 1.95, 3.90, 5.08, and 7.80 mm for the relative dielectric constant of $\varepsilon_{rB} = 10$ and the wafer-focus ring gap of $\Delta r_2 = 2$ mm.

(e + Ar → 2e + Ar$^+$), and two types of Ar$^+$-Ar collisions: elastic (Ar$^+$+Ar → Ar$^+$+Ar) and charge exchange (Ar$^+$+Ar → Ar + Ar$^+$). The corresponding cross sections are from Ref. 35. Secondary electron emission and electron reflection at boundary surfaces are not considered for simplicity. The discharge is studied by applying voltage waveform, $V_{rf}(t) = V\cos(2\pi ft)$, where $f = 27.12$ MHz and $V = 300$ V. The number of cells is 128 in the z-direction and 650 in the r-direction, and both the space step Δr and Δz are set at 1.95×10^{-4} m. The numerical time step Δt is taken to be 5×10^{-11} s. All the presented plasma parameters in this work are calculated after the simulations reach equilibrium by repeating around 1000 RF cycles.

III. RESULTS AND DISCUSSION

A. Effects of the focus ring height

Figure 4 shows the time-averaged electron density profiles for the focus ring heights of $h_B = 1.95$, 3.90, 5.08, and 7.80 mm. The relative dielectric constant is set at $\varepsilon_{rB} = 10$, and the wafer-focus ring gap is fixed at $\Delta r_2 = 2$ mm. It is evident that under the influence of a negative DC self-bias voltage, the electron density profiles are displaced away from the bottom electrode. Besides, the discharge can be roughly divided into two regions at about $r = 9$ cm, i.e., one region above the wafer and one region on the right side of the wafer. The discharge above the wafer is mainly sustained by the RF power applied on the bottom electrode, whereas the discharge on the right side of the wafer is generated by stochastic heating, resulting from the oscillating RF sheath at the grounded chamber sidewall. Furthermore, the electric potential profile exhibits a slight curvature in the vicinity of the area between the wafer and the focus ring, as depicted in Fig. 5, which displays the time-averaged distributions of electric potential and horizontal electric field. When the focus ring is positioned below the wafer, the highest density is observed on the right side of the wafer, as illustrated in

28 July 2023 00:26:18

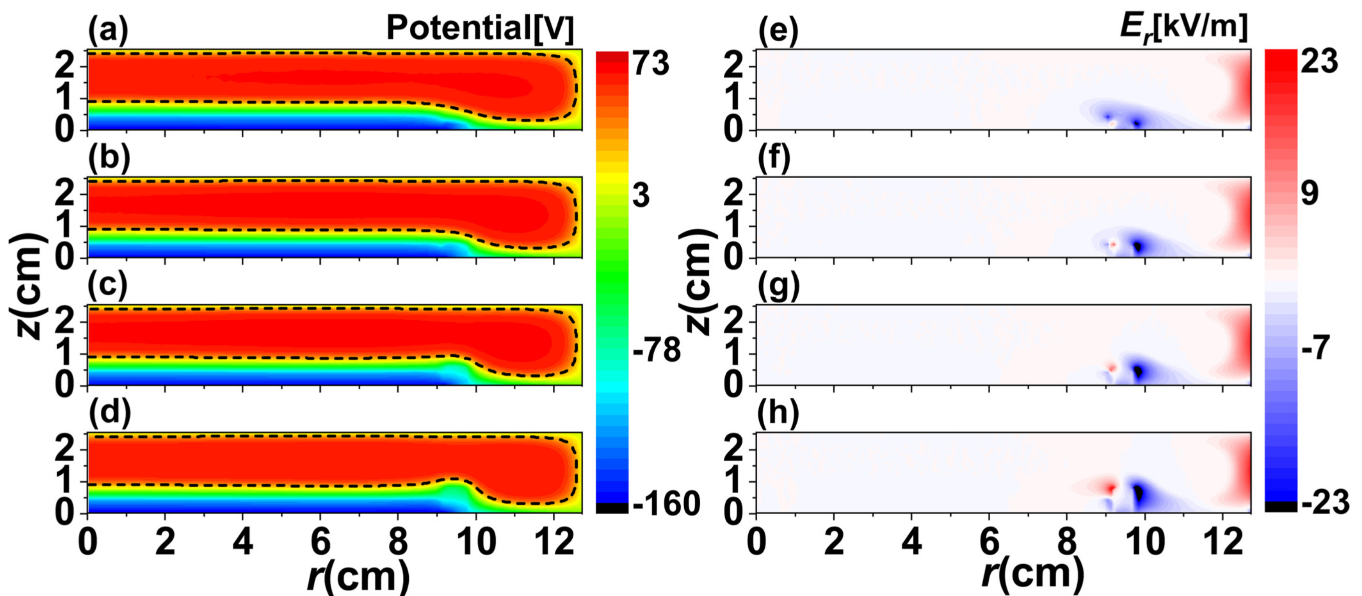

FIG. 5. Time-averaged profiles of (a)–(d) the electric potential and (e)–(h) the horizontal electric field are shown for the relative dielectric constant of $\varepsilon_{rB} = 10$ and the wafer-focus ring gap of $\Delta r_2 = 2$ mm. First row: $h = 1.95$ mm; second row: $h = 3.90$ mm; third row: $h = 5.08$ mm; fourth row: $h = 7.80$ mm. The black dashed lines in (a)–(d) are the equipotential lines with the electric potential of 32 V. The positive electric field points to the right direction.

Published under an exclusive license by the AVS

Fig. 4(a). This can be attributed to strong electric fields induced by both sharp edges of the wafer and the focus ring, as evidenced by blue color in Fig. 5(e), which intensify the discharge. When the focus ring is slightly elevated to match the height of the wafer [as shown in Fig. 4(b)], the electric field at the edge of the wafer decreases. However, the skewed sheath edge of the right side of the focus ring still induces a strong electric field, as depicted in Figs. 5(b) and 5(f), causing a slight shift in the density peak toward the right direction. When the focus ring is slightly higher than the wafer [as depicted in Fig. 4(c)], the bulk plasma region above the focus ring becomes compressed, which results in a visible split in the discharge. As the height of the focus ring is further increased, the horizontal electric fields at the edges of the focus ring continue to intensify, as shown in Figs. 5(d) and 5(h). These horizontal electric fields push the plasma in opposite directions, resulting in the formation of two distinct density peaks on both sides of the focus ring, as illustrated in Fig. 4(d). Furthermore, the electric field induced by the sharp edges of the wafer and focus ring has a

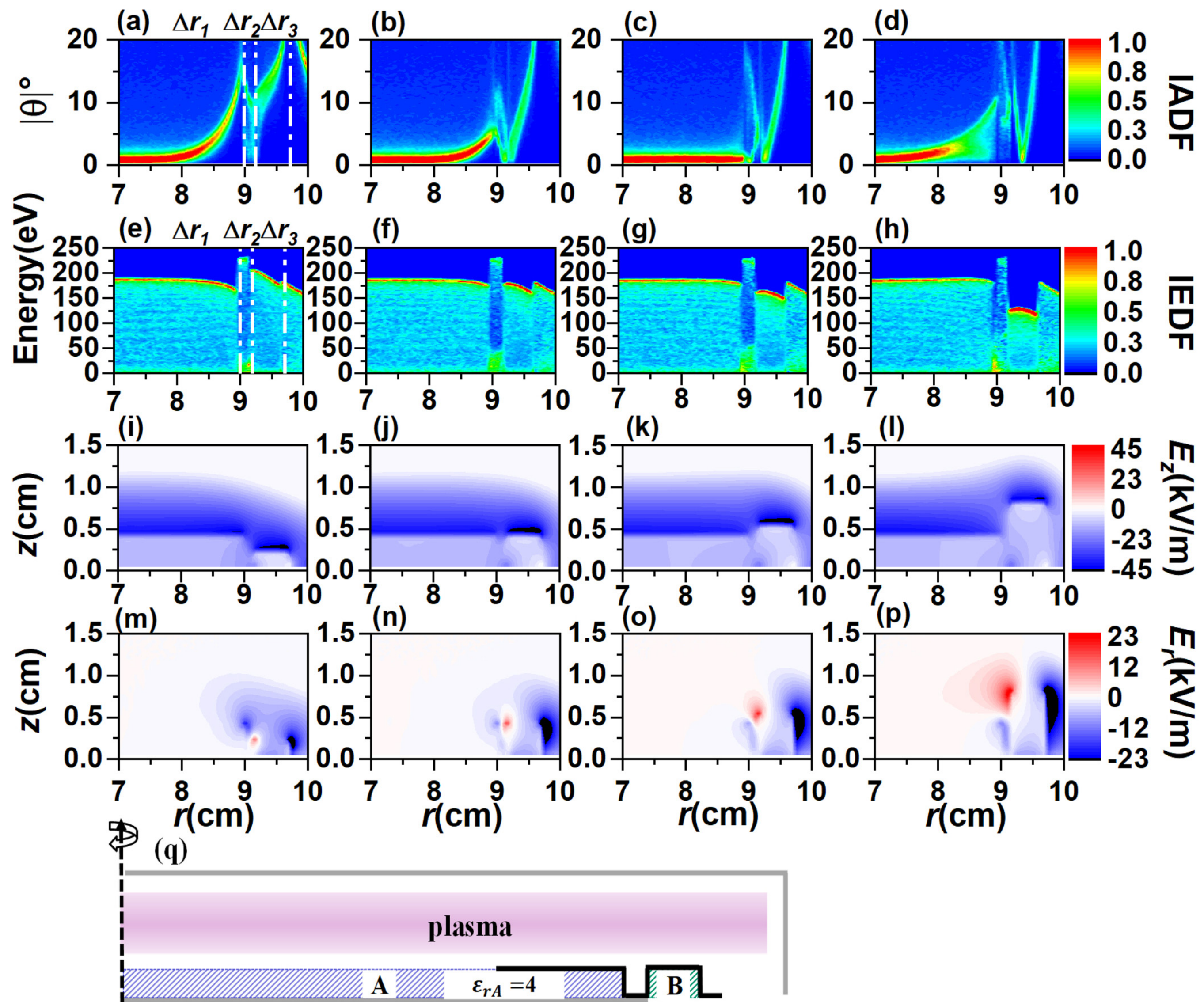

FIG. 6. Time-averaged plots of (a)–(d) IADF, (e)–(h) IEDF, (i)–(l) the vertical electric field E_z, and (m)–(p) the horizontal electric field E_r (r = 7–10cm), when the relative dielectric constant of the focus ring ε_{rB} is set as 10 and the wafer-focus ring gap Δr_2 is set as 2 mm. First column: h = 1.95 mm; second column: h = 3.90 mm; third column: h = 5.08 mm; fourth column: h = 7.80 mm. The black solid line of (q) is the statistic position of the IEDF and IADF (i.e., the horizontal location along the geometry surface). The positive electric field E_z points to the upper direction and the positive electric field E_r points to the right direction.

28 July 2023 00:26:18

Published under an exclusive license by the AVS

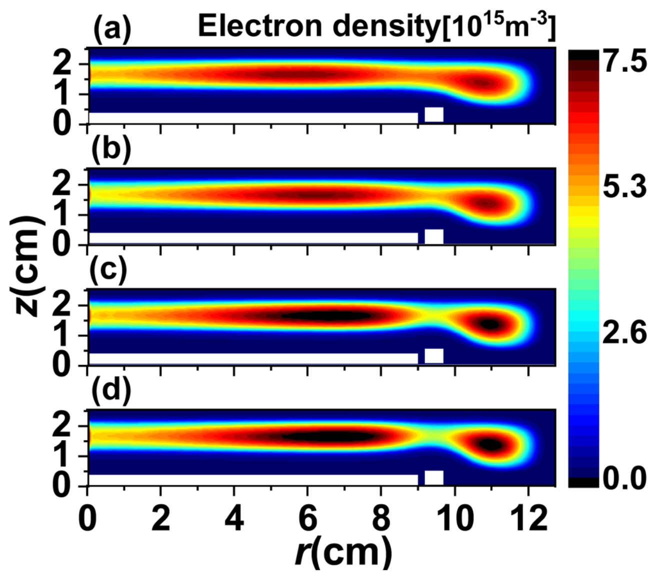

FIG. 7. Time-averaged profiles of (a)–(d) the electron density with the relative dielectric constants of $\varepsilon_{rB} = 2$, 6, 20, and 40 for the focus ring height of $h_B = 5.85$ mm and the wafer-focus ring gap of $\Delta r_2 = 2$ mm.

significant impact on ion trajectories near the edge of the wafer. To further analyze the ion kinetics, we plot IADF, IEDF, and electric field components ($E_z$andE_r) near the wafer edge ($r = 7$–10 cm) in Fig. 6.

The ion angles |θ| in Figs. 6(a)–6(d) represent the absolute values of the ions bombarding angle, where $|\theta| = 0$ corresponds to the direction normal to the wafer surface. At $r < 7.5$ cm, the IADFs are mostly uniform with small ions bombarding angle, indicating that the ions are nearly vertically bombarding the wafer surface under the acceleration effect of E_z for all cases. While the IADFs exhibit significant nonuniformity with large ions bombarding angle |θ| at the wafer edge [r = 7.5–9 cm, see Fig. 6(a)] when the focus ring is lower than the wafer. This nonuniformity arises from the negative electric field E_r (blue color) in the horizontal direction induced by the sharp edge of the wafer, which leads to the deflection of ions toward the left direction with a maximum angle of 19°. When the focus ring is raised to the same height as the wafer, the E_r at the wafer edge is significantly reduced [see Fig. 6(n)] due to the reduced distortion of the sheath near the wafer edge [see Fig. 5(b)], inducing smaller ions' bombarding angle |θ| [see Fig. 6(b)]. As the focus ring is further elevated, it can be noticed that a strong positive electric field E_r (red color) is developed at the inner (left) edge of the focus ring [see Fig. 5(c)], which counteracts the negative electric field E_r (blue color) at the wafer edge to some extent, so the ions are nearly vertically bombarding the wafer edge [$r = 7.5$–9 cm, see Fig. 6(c)]. However, as the focus ring continues to rise, the positive electric field at the inner edge of the focus ring becomes even stronger [see Fig. 6(p)], causing the ions to be reversely deflected toward the right direction, which induces a large bombarding angle |θ| [see Fig. 6(d)].

Noting that the maximum energy of the ions bombarding the focus ring is inversely proportional to the height h_B of the focus ring approximately in Figs. 6(e)–6(h) ($r = 9.2$–9.7 cm). This is

28 July 2023 00:26:18

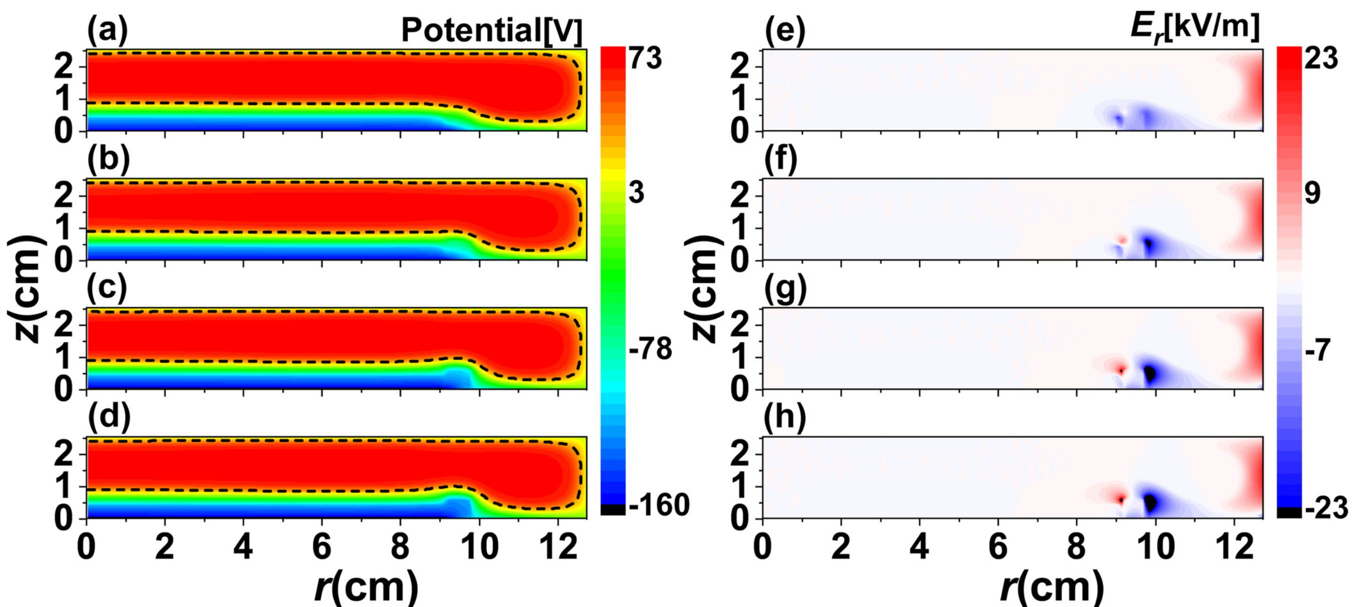

FIG. 8. Time-averaged profiles of (a)–(d) the electric potential and (e)–(h) the horizontal electric field are shown for the focus ring height of $h_B = 5.85$ mm and the wafer-focus ring gap of $\Delta r_2 = 2$ mm. First row: $\varepsilon_{rB} = 2$; second row: $\varepsilon_{rB} = 6$; third row: $\varepsilon_{rB} = 20$; fourth row: $\varepsilon_{rB} = 40$. The black dashed lines in (a)–(d) are equipotential lines with the electric potential of 32 V.

Published under an exclusive license by the AVS

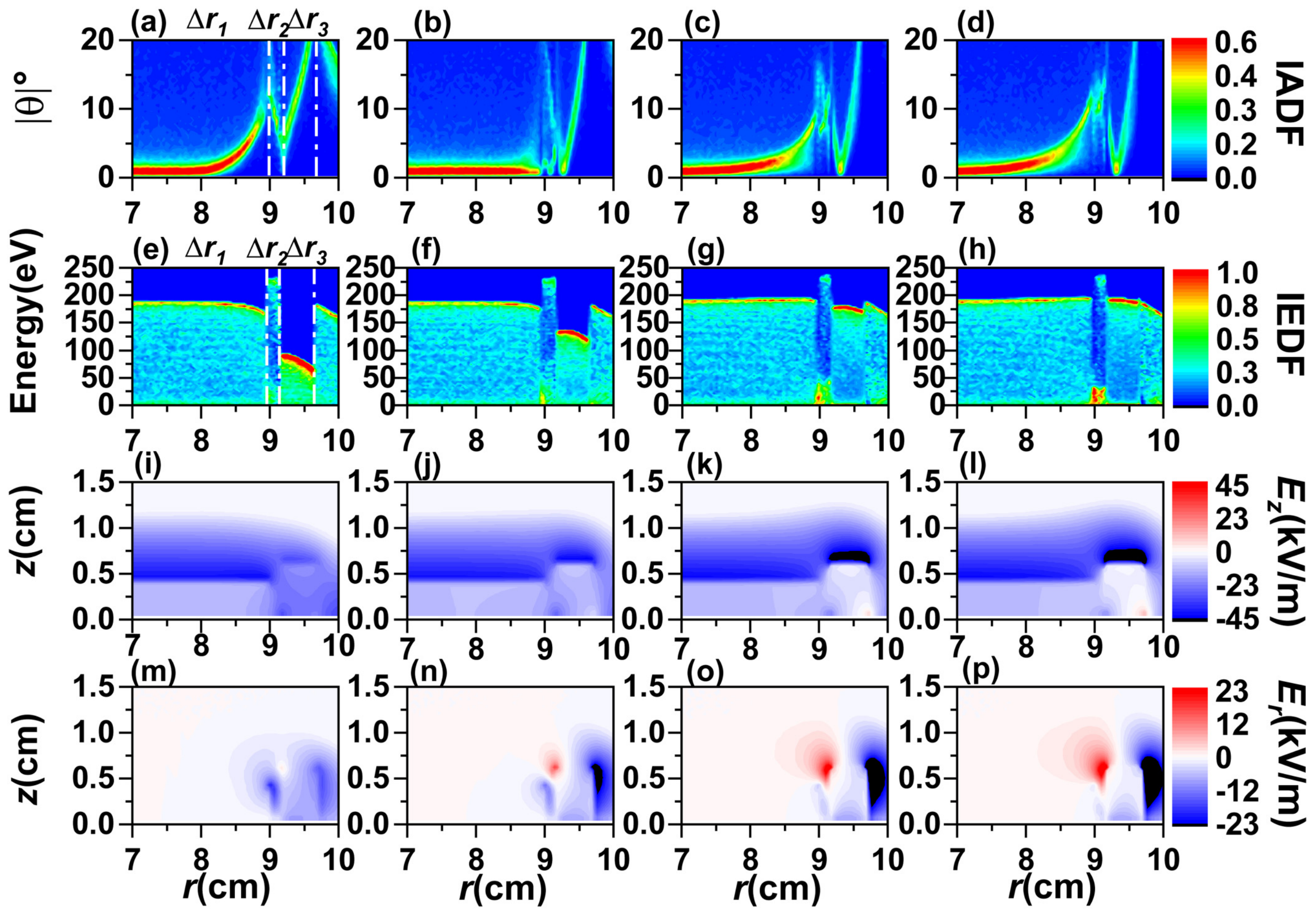

FIG. 9. Time-averaged plots of (a)–(d) IADF, (e)–(h) IEDF, (i)–(l) vertical electric field E_z, and (m)–(p) horizontal electric field E_r near the focus ring ($r = 7$–10 cm), when the focus ring height h_B is set as 5.85 mm and the wafer-focus ring gap Δr_2 is set as 2 mm. First column:$\varepsilon_{rB} = 2$; second column: $\varepsilon_{rB} = 6$; third column: $\varepsilon_{rB} = 20$; fourth column: $\varepsilon_{rB} = 40$.

28 July 2023 00:26:18

because the equivalent impedance components consist of the focus ring, sheath, and bulk plasma. The capacitance of the focus ring decreases and the impedance increases with rising h_B, which may lead to a higher voltage drop across the focus ring and a smaller sheath voltage above it. As a result, the ion energy bombarding the focus ring decreases. Additionally, the degradation of the spatial potential away from the electrode edge plays a role in reducing the ions' bombarding energy along the focus ring surface. This can be observed by the presence of "slope" IEDF profiles on the surface of the focus ring.

To conclude, maintaining a slightly higher focus ring than the wafer results in both small ions bombarding angles at the wafer edge and reduced ions bombarding energies on the focus ring surface. This combination promotes desirable etching profiles and extends the lifespan of the focus ring for specific discharge parameters investigated in this study.

B. Examinations on the dielectric constant of the focus ring

The spatial distributions of the time-averaged electron density with the variation of the relative dielectric constants $\varepsilon_{rB} = 2, 6, 20,$ and 40 of the focus ring are shown in Fig. 7, in which the focus ring height and the wafer-focus ring gap are set as $h_B = 5.85$ mm and $\Delta r_2 = 2$ mm, respectively. The discharge region can still be roughly divided into two regions. The impedance of the focus ring decreases with increasing the dielectric constant, which leads to a less voltage drop across the focus ring and a larger sheath potential. Therefore, the sheath over the focus ring thickens, and the horizontal electric fields at both the left and the right sides of the focus ring enhance due to a more pronounced sheath distortion at about $r = 9$ cm, as seen in Fig. 8, which presents the time-averaged electric potential and horizontal electric field distributions. As a result, similar to the conclusion drawn in Fig. 4, the

Published under an exclusive license by the AVS

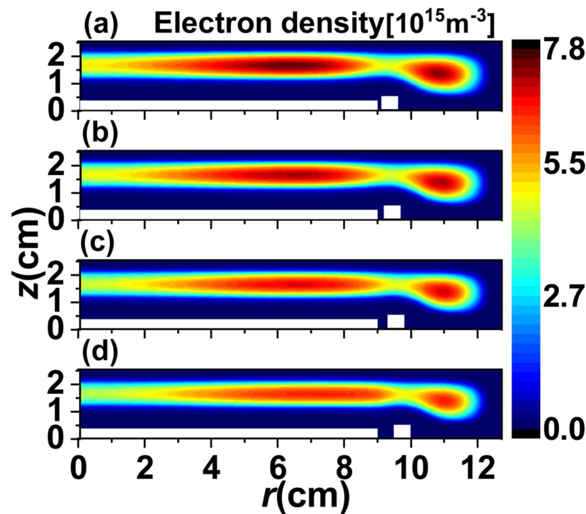

FIG. 10. Time-averaged plots of (a)–(d) the electron density with the wafer-focus ring gap of $\Delta r_2 = 0.39$, 2, 3, and 5 mm for the height $h_B = 5.85$ mm and the relative dielectric constant $\varepsilon_{rB} = 10$ of the focus ring.

densities in both plasma regions separated by the focus ring increase due to enhanced electric field with rising the dielectric constant of the focus ring.

Figure 9 illustrates IADF (a)–(d), IEDF (e)–(h), the vertical electric field E_z (i)–(l), and the horizontal electric field E_r (m)–(p), when the relative dielectric constants ε_{rB} are set as 2, 6, 20, and 40, respectively. In Figs. 9(a)–9(d), the ions nearly vertically bombard the wafer surface at $r < 7.5$ cm, under the acceleration effect of E_z [see Figs. 9(i)–9(l)]. As the strong negative electric field E_r is induced by the sharp edge of the wafer at $\varepsilon_{rB} = 2$ [see Fig. 9(m)], the ions will be deflected toward the left direction, resulting in a large bombarding angle $|\theta|$ at $r = 7.5$–9 cm [see Fig. 9(a)]. As the relative dielectric constant increases to 6 [see Fig. 9(n)], a strong positive electric field E_r (red color) develops at the inner edge of the focus ring, which counteracts the negative electric field E_r (blue color) at the wafer edge to some extent, inducing a reduced bombarding angle $|\theta|$ near the wafer edge ($r = 7.5$–9 cm) as shown in Fig. 9(b). However, the positive electric field E_r (red color) at the inner edge of the focus ring becomes so strong with further increasing the ε_{rB} [see Figs. 9(o) and 9(p)], that the ions are reversely deflected toward the right, inducing a slightly increased bombarding angle $|\theta|$ again [see Figs. 9(c) and 9(d)].

In Figs. 9(e)–9(h), the maximum energy of the ions bombarding the focus ring ($r = 9.2$–9.7 cm) is approximately proportional to the relative dielectric constants ε_{rB} of the focus ring. This is because the local impedance of the focus ring reduces with increasing ε_{rB}, leading to a less potential drop across the focus ring and a larger potential drop in the sheath. As a result, the ion energy bombarding the focus ring increases with rising the dielectric constant of the focus ring.

C. How the wafer-focus ring gap affects the edge plasma

The spatial distributions of the time-averaged electron density are shown in Fig. 10 for $\Delta r_2 = 0.39$, 2, 3, and 5 mm, respectively. The focus ring height h_B is set as 5.85 mm and the relative

28 July 2023 00:26:18

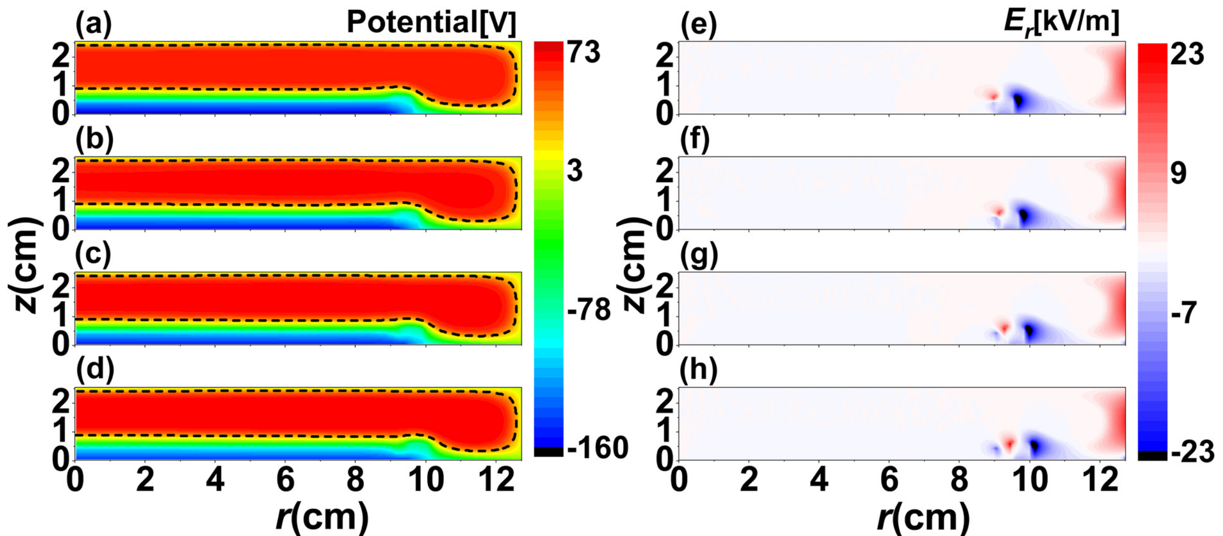

FIG. 11. Time-averaged profiles of (a)–(d) the electric potential and (e)–(h) the horizontal electric field are shown for the focus ring height of $h_B = 5.85$ mm and the relative dielectric constant $\varepsilon_{rB} = 10$ of the focus ring. First row:$\Delta r_2 = 0.39$ mm; second row: $\Delta r_2 = 2$ mm; third row: $\Delta r_2 = 3$ mm; fourth row: $\Delta r_2 = 5$ mm. The black dashed lines in (a)–(d) are the equipotential lines with the electric potential of 32 V.

Published under an exclusive license by the AVS

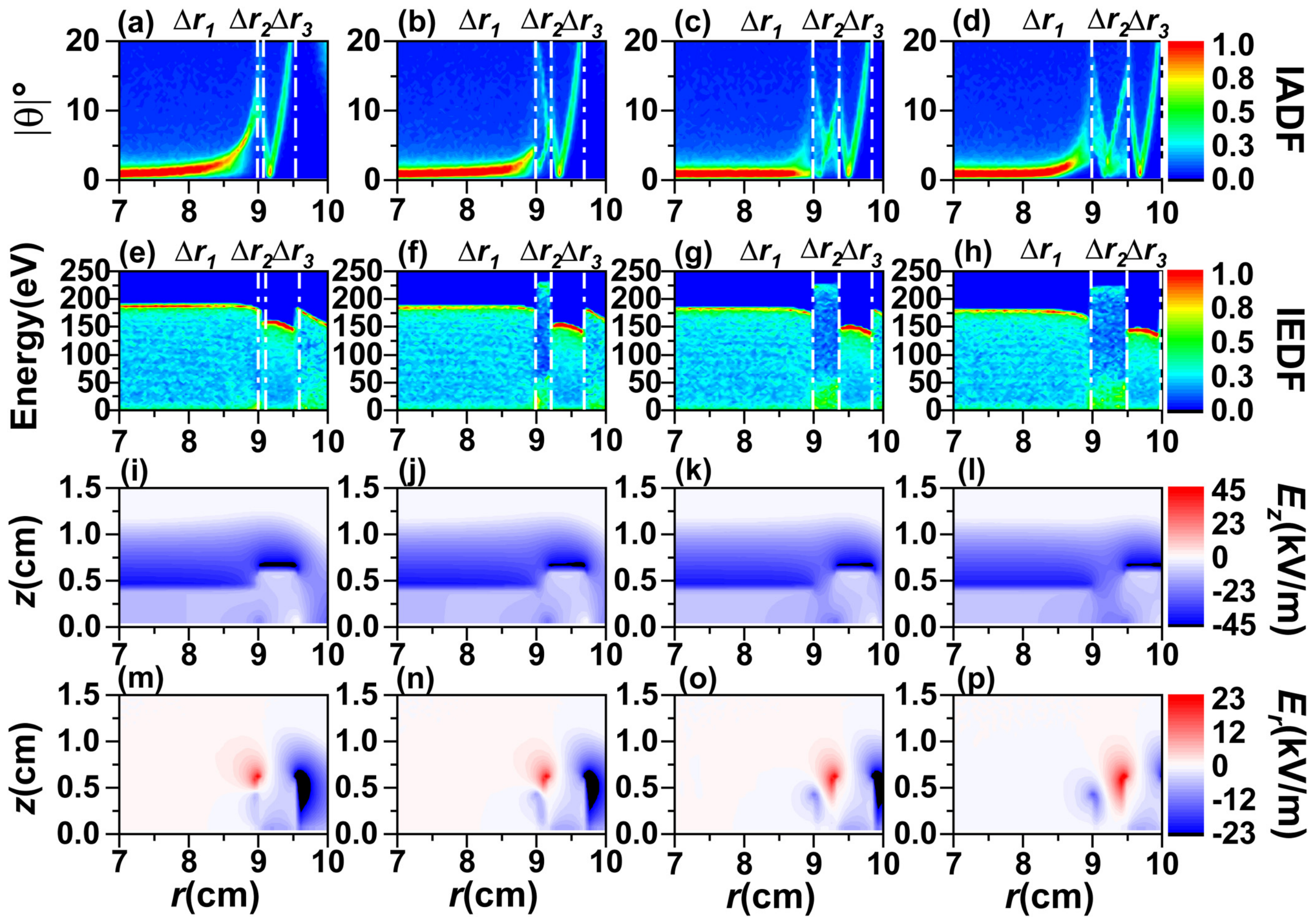

FIG. 12. Time-averaged plots of (a)–(d) IADF, (e)–(h) IEDF, (i)–(l) vertical electric field E_z, and (m)–(p) the horizontal electric field E_r ($r = 7$–10 cm), when the focus ring height h_B is set as 5.85 mm, and the wafer-focus ring gap ε_{rB} is set as 10. First column:$\Delta r_2 = 0.39$ mm; second column: $\Delta r_2 = 2$ mm; third column: $\Delta r_2 = 3$ mm; fourth column $\Delta r_2 = 5$ mm.

28 July 2023 00:26:18

dielectric constant ε_{rB} is fixed at 10. As Δr_2 increases (i.e., the focus ring gradually shifts toward the right), the effective discharge region on the right of the focus ring is reduced, resulting in a lower electron density in this region [see Figs. 10(a)–10(d)]. Figure 11 shows the time-averaged electric potential and horizontal electric field. Increasing the width of the gap allows the plasma to penetrate more easily into the wafer-focus ring gap, causing the equipotential lines to bend near the region between the wafer and the focus ring. This, in turn, distorts the sheath [see Figs. 11(a)–11(d)]. Consequently, strong electric fields are induced at both the wafer edge and the left side of the focus ring due to the distorted sheath edge [see the strong red and blue color regions in Figs. 11(e)–11(h)]. The intensified electric field leads to an increased electron density at about $r = 9$ cm. Accordingly, the two plasma regions separated by the focus ring tend to merge with each other as the wafer-focus ring gap widens.

Figure 12 further shows IADF (a)–(d), IEDF (e)–(h), the vertical electric field E_z (i)–(l), and the horizontal electric field E_r (m)–(p) for different wafer-focus ring gaps ($\Delta r_2 = 0.39$ 0.39, 2, 3, and 5 mm). When the wafer-focus ring gap is very small ($\Delta r_2 = 0.39$ mm), the ions impinging on the wafer edge are slightly deflected to the right direction due to the effect of the stronger positive electric field E_r at the inner side of the focus ring [see Figs. 12(a) and 12(m)]. As the gap increases to 2 mm, the inner side of the focus ring moves slightly further away from the wafer edge. This weakens the effect of the electric field at the inner side of the focus ring, resulting in a smaller angle of ion bombardment. In particular, when the gap is 3 mm, the positive electric field (indicated by the red color) at the inner edge of the focus ring is partially counteracted by the negative electric field (indicated by the blue color) at the wafer edge. As a result, the ions tend to bombard the wafer edge at a perpendicular angle. When the gap further

Published under an exclusive license by the AVS

increases to 5 mm, the electric field induced by the sharp edge of the wafer becomes dominant in determining the ion trajectories. Consequently, the incident ions on the wafer edge are deflected to the left with an increased impact angle $|\theta|$.

The maximum energy of the ions bombarding the focus ring remains almost unaffected as the gap increases because the impedance of the focus ring remains relatively constant.

IV. CONCLUSIONS

A self-consistent 2D3V PIC/MCC model was employed to examine the impact of the focus ring near the wafer edge on the plasma characteristics. Specifically, the study focused on the IADF on the wafer edge and the IEDF on the focus ring at a pressure of 20 mTorr.

The investigation revealed that the height and relative dielectric constant of the focus ring significantly affect the plasma discharge. Increasing these parameters leads to the compression of the bulk plasma region directly above the focus ring, resulting in the division of the discharge region into two distinct parts. Furthermore, widening the gap between the wafer and the focus ring causes a decrease in the effective discharge region on the right side of the focus ring, leading to a sharp decline in electron density within this area.

The IADFs are mostly uniform for $r < 7.5$ cm with small ions bombarding angle, indicating that the ions are bombarding the wafer in a nearly vertical direction. However, in the range of $r = 7.5$–9 cm, significant nonuniformities in the IADFs are observed due to the negative electric field induced by the sharp edge of the wafer, deflecting ions.

Moreover, the ion trajectories near the wafer edge were found to be influenced by an additional positive electric field at the inner edge of the focus ring. This positive electric field, which increases with the height or dielectric constant of the focus ring, interacts with the negative electric field induced by the wafer, even resulting in a uniform and optimized IADF at the wafer edge. Additionally, it was observed that reducing the height and increasing the dielectric constant of the focus ring elevated the capacitance and lowered the impedance. Consequently, this may lead to an increased sheath potential drop and higher ion energy bombarding the focus ring.

It is worth noting that the primary objective of this study is to investigate the influence of the focus ring on ion dynamics near the wafer edge. For the sake of simplicity, a single-frequency discharge was applied in this work. The impact of the focus ring in a dual-frequency discharge will be explored in future research.

ACKNOWLEDGMENTS

This work was financially supported by the National Natural Science Foundation of China (NSFC) (Grant Nos. 12105035 and 11935005), the Guangdong Basic and Applied Basic Research Foundation (Grant No. 2021B1515120018), the Fundamental Research Funds for the Central Universities (No. DUT21TD104), and the Advanced Space Propulsion Laboratory of BICE and Beijing Engineering Research Center of Efficient and Green Aerospace Propulsion Technology (No. LabASP-2020-01).

AUTHOR DECLARATIONS

Conflict of Interest

The authors have no conflicts to disclose.

Author Contributions

Fang-Fang Ma: Conceptualization (equal); Data curation (equal); Formal analysis (equal); Investigation (equal); Writing – original draft (equal). **Quan-Zhi Zhang:** Conceptualization (equal); Formal analysis (equal); Investigation (equal); Writing – review & editing (equal). **Dao-Man Han:** Investigation (equal); Writing – review & editing (equal). **Zi-Lan Xiong:** Investigation (equal); Writing – review & editing (equal). **Ming Gao:** Investigation (equal); Writing – review & editing (equal). **You-Nian Wang:** Investigation (equal); Supervision (equal); Writing – review & editing (equal).

DATA AVAILABILITY

The data that support the findings of this study are available from the corresponding author upon reasonable request.

REFERENCES

[1]M. A. Lieberman and A. J. Lichtenberg, *Principles of Plasma Discharges and Materials Processing*, 2nd ed. (Wiley, New York, 2005).
[2]M. Y. Hur, J. S. Kim, I. C. Song, J. P. Verboncoeur, and H. J. Lee, Plasma Res. Express **1**, 015016 (2019).
[3]C. G. N. Lee, K. J. Kanarik, and R. A. Gottscho, J. Phys. D: Appl. Phys. **47**, 273001 (2014).
[4]K. Nojiri, *Dry Etching Technology for Semiconductors* (Springer International Publishing, New York, 2015).
[5]E. V. Barnat and G. A. Hebner, J. Appl. Phys. **96**, 4762 (2004).
[6]E. V. Barnat and G. A. Hebner, J. Appl. Phys. **98**, 013305 (2005).
[7]K. Denpoh and T. Shirafuji, Jpn. J. Appl. Phys. **50**, 036001 (2011).
[8]D. Kim and D. J. Economou, J. Appl. Phys. **94**, 2852 (2003).
[9]M. J. Kushner, J. Phys. D: Appl. Phys. **42**, 194013 (2009).
[10]D. Kim and D. J. Economou, J. Appl. Phys. **95**, 3311 (2004).
[11]D. Kim, D. J. Economou, J. R. Woodworth, P. A. Miller, R. J. Shul, B. P. Aragon, T. W. Hamilton, and C. G. Willison, IEEE Trans. Plasma Sci. **31**, 691 (2003).
[12]E. V. Barnat and G. A. Hebner, J. Appl. Phys. **97**, 063301 (2005).
[13]M. Y. Yoon, H. J. Yeom, J. H. Kim, J. R. Jeong, and H. C. Lee, Appl. Surf. Sci. **595**, 153462 (2022).
[14]I. Seong, J. Lee, S. Kim, Y. Lee, C. Cho, J. Lee, W. Jeong, Y. You, and S. You, Nanomaterials **12**, 3963 (2022).
[15]X. Wang, H. Lee, S. K. Nam, and M. J. Kushner, J. Vac. Sci. Technol. A **39**, 063002 (2021).
[16]L. Tong, Jpn. J. Appl. Phys. **54**, 06GA01 (2015).
[17]K. Denpoh and T. Shirafuji, Jpn. J. Appl. Phys. **49**, 056202 (2010).
[18]N. Y. Babaeva and M. J. Kushner, J. Appl. Phys. **101**, 113307 (2007).
[19]J. S. Kim, M. Y. Hur, H. J. Kim, and H. J. Lee, J. Appl. Phys. **126**, 233301 (2019).
[20]N. Y. Babaeva and M. J. Kushner, J. Phys. D: Appl. Phys. **41**, 062004 (2008).
[21]H. Y. Wang, W. Jiang, and Y. N. Wang, Plasma Sources Sci. Technol. **19**, 045023 (2010).
[22]J. Schulze, E. Schüngel, Z. Donkó, and U. Czarnetzki, J. Phys. D: Appl. Phys. **43**, 225201 (2010).
[23]B. G. Heil, U. Czarnetzki, R. P. Brinkmann, and T. Mussenbrock, J. Phys. D: Appl. Phys. **41**, 165202 (2008).
[24]E. Bultinck, I. Kolev, A. Bogaerts, and D. Depla, J. Appl. Phys. **103**, 013309 (2008).

28 July 2023 00:26:18

Published under an exclusive license by the AVS

[25]V. Vahedi and G. Dipeso, J. Comput. Phys. **131**, 149 (1997).
[26]S. Wilczek, J. Trieschmann, J. Schulze, Z. Donkó, R. P. Brinkmann, and T. Mussenbrock, Plasma Sources Sci. Technol. **27**, 125010 (2018).
[27]J. Y. Sun, Q. Z. Zhang, and Y. N. Wang, Phys. Plasmas **28**, 013509 (2021).
[28]T. Mussenbrock, R. P. Brinkmann, M. A. Lieberman, A. J. Lichtenberg, and E. Kawamura, Phys. Rev. Lett. **101**, 085004 (2008).
[29]B. Bora, H. Bhuyan, M. Favre, E. Wyndham, and H. Chuaqui, Appl. Phys. Lett. **100**, 094103 (2012).
[30]U. Czarnetzki, J. Schulze, E. Schüngel, and Z. Donkó, Plasma Sources Sci. Technol. **20**, 024010 (2011).
[31]Q. Z. Zhang, S. X. Zhao, W. Jiang, and Y. N. Wang, J. Phys. D: Appl. Phys. **45**, 305203 (2012).
[32]Y. X. Liu, Y. S. Liang, D. Q. Wen, Z. H. Bi, and Y. N. Wang, Plasma Sources Sci. Technol. **24**, 025013 (2015).
[33]L. Lauro-Taroni, M. M. Turner, and N. S. J. Braithwaite, J. Phys. D: Appl. Phys. **37**, 2216 (2004).
[34]M. Roberto, H. B. Smith, and J. P. Verboncoeur, IEEE Trans. Plasma Sci. **31**, 1292 (2003).
[35]A. V. Phelps and Z. L. Petrović, Plasma Sources Sci. Technol. **8**, R21 (1999).

28 July 2023 00:26:18

Published under an exclusive license by the AVS